Journal of the European Ceramic Society **19** (1999) 1631–1639

PII: S0955-2219(98)00258-1
0955-2219/99/$ - see front matter

Measuring the Anisotropic Thermal Diffusivity of Silicon Nitride Grains by Thermoreflectance Microscopy

Bincheng Li,[a,*] L. Pottier,[a,†] J. P. Roger,[a] D. Fournier,[a] K. Watari[b] and K. Hirao[b]

[a]Laboratoire d'Instrumentation de l'Université Pierre et Marie Curie, UPR A0005 du CNRS, 10 rue Vauquelin, F-75005 Paris, France
[b]National Industrial Research Institute of Nagoya, Hirate-cho 1-1, Kita-ku, Nagoya 462, Japan

(Received 26 May 1998; accepted 10 October 1998)

Abstract

High-resolution thermoreflectance microscopy measurements were performed at five frequencies on rod-shaped Si_3N_4 grains in a ceramic. Our heat diffusion model takes account of the coating and of a coating/substrate resistance. The parameters are adjusted to fit the measurements at the five frequencies simultaneously. The principal diffusivities obtained in individual grains are 0·32 $cm^2 s^{-1}$ along the a*-axis, and 0·84 $cm^2 s^{-1}$ along the* c*-axis (corresponding conductivities: 69 and 180 $W m^{-1} K^{-1}$). The thermal anisotropy inside individual Si_3N_4 grains is found to be intrinsic, without direct connection with their elongated shape. 'Macroscopic' diffusivities, obtained by mirage effect, are different from the values measured inside individual grains, as a consequence of the dispersion of the grains' orientations in the ceramic and of a second-phase effect.*

Keywords: non-destructive evaluation, thermal conductivity, Si_3N_4, photoreflectance microscopy.

1 Introduction

Since the 80s, numerous photothermal techniques have been developed and widely applied to the thermal characterisation of various materials. Many works dealt with measurements of the thermal diffusivity of isotropic materials[1–3] or isotropic thin films.[4–6] Recently several works were devoted to measurements of the thermal diffusivity of *anisotropic* materials.[7–13] Among the photothermal techniques used for thermal diffusivity measurements, the mirage method is a very good tool for '*macroscopic*' measurements, while modulated thermoreflectance microscopy is more appropriate for *local* measurements. The high spatial resolution of thermoreflectance microscopy makes it very suitable to measure the thermal behaviour of individual grains whose sizes range from a few microns to a few tens of microns. Of course, the modulation frequency has to be chosen high enough to restrict the thermal flux to the region of interest, e.g. inside one individual grain.

Reliable thermoreflectance measurements require the reflectance (and the reflectance's temperature coefficient) of the material to be sufficiently high. Therefore, in the case of non-metallic solids, the surface has usually to be coated with a thin film of metal (typically: a gold film of several tens of nanometers) to provide sufficient thermoreflectance signals. Due to imperfect thermal contact between the coating and the material, there is usually a thermal resistance at the interface. This thermal resistance, as well as the thermophysical properties of the film (often quite different from those of the corresponding bulk material), strongly influence heat diffusion on the surface of the sample at high modulation frequency. As a result, the substrate's diffusivity cannot be extracted from the thermoreflectance measurements by means of the widely used simple methods.[2] A heat diffusion model including the thin film and the thermal boundary resistance has to be used, and the substrate's diffusivity is extracted by some fitting process.

On the other hand, Si_3N_4 ceramics are excellent candidates for high-temperature structural materials, owing to their outstanding mechanical and chemical properties at elevated temperatures. Recently, due to improvements of their thermal

*Present address: Institut für Optik und Quantenelektronik, Friedrich-Schiller Universität Jena, Max-Wien Platz 1, D-07743 Jena, Germany.
†To whom correspondence should be addressed. Fax: +33-1-43-36-23-95; e-mail: pottier@optique.espci.fr

conductivity, they have aroused considerable interest as potential candidates to make high-performance substrates for semiconductor devices. Values up to $200\,W\,m^{-1}\,K^{-1}$ have been estimated for the intrinsic thermal conductivity of Si_3N_4.[14] Commonly measured values range from 10 to $70\,W\,m^{-1}\,K^{-1}$, depending on the sintering method. Some time ago Hirosaki *et al.*[15] and Hirao *et al.*[16] demonstrated that the thermal conductivity of Si_3N_4 ceramics can be increased to $120\,W\,m^{-1}\,K^{-1}$ or even higher.[17] Recently, Si_3N_4 ceramic with a thermal conductivity of $155\,W\,m^{-1}\,K^{-1}$ was obtained using an ultra-high temperature, hot isostatic pressing (HIP) process.[17] The same authors also observed thermal anisotropy, and demonstrated that the thermal properties of sintered Si_3N_4 ceramics are closely related to the behaviour of the grain growth. Measurements of the thermal conductivity inside individual Si_3N_4 grains would be helpful to understand and improve the thermal conductivity of Si_3N_4 ceramics.

In the present work, we apply the thermoreflectance microscopy technique to determine the thermal diffusivities of individual Si_3N_4 grains, and the mirage method to measure the macroscopic diffusivities of Si_3N_4 samples averaged over many grains. The dependence of the amplitude and of the phase on the separation between the two beams is recorded, at different modulation frequencies, along the two principal axes located in the surface plane. The principal thermal diffusivities of the Si_3N_4 grains are determined by fitting to the measurements the numerical values injected into a proper heat diffusion model. The macroscopic values are extracted from the behaviour of the phase of the transverse probe beam deflection using the phase method.[18]

2 Experimental Method; Samples

The experimental set-up of the thermoreflectance microscope, similar to that of Refs 19 and 20, is described in detail elsewhere.[21] In brief, an intensity-modulated Ar^+ laser beam focused by an optical microscope onto the surface of the sample excites a thermal wave. The resulting distribution of the surface temperature modulation is read by a second laser beam via thermoreflectance. The amplitude and the phase of the thermoreflectance signal are extracted by lock-in detection. The mirage set-up is described elsewhere.[22,23]

The Si_3N_4 ceramic samples were fabricated by tape-casting of α-Si_3N_4 powder with 5% Y_2O_3 and 5 vol% rodlike β-Si_3N_4 seed particles, followed by tape stacking, hot-pressing at a temperature of 1800 °C for 2 h, and hot isostatic pressing (HIPing) at 2500 °C for 2 h. (The preparation procedure of the sample is described in detail in Refs 16 and 17.) The samples exhibit a highly anisotropic microstructure (Fig. 1) with long rods of β-Si_3N_4 (developed from seed particles). In the tape-casting process, each rod has to accommodate itself inside the limited thickness of the tape. As a result, viewed on face B (Fig. 1), the rods are essentially parallel to the tape-casting direction. Viewed from face C, the rods exhibit again a favoured orientation along the tape-casting direction. Yet the orientation dispersion is much larger, because the dimension of the tape perpendicularly to the casting direction is much larger for face C than for face B. Face A mainly exhibits rounded orthogonal cross-sections, plus a few somewhat elongated oblique sections.

The structure of β-Si_3N_4 is hexagonal. Consequently, the diffusivity tensor is uniaxial, and its favoured axis is the *c*-axis of the crystal. All directions normal to the *c*-axis are thermally equivalent to an *a*-axis. Therefore, we shall from now on call them all 'thermal *a*-axes'. The longitudinal axis of the rod coincides with the crystal's *c*-axis, and the density of defects in the rods is low.[16] The size varies from rod to rod, with a length range of 10–150 μm and a diameter range of 2–20 μm. Some Si_3N_4 is also present as small particles in the second phase between the rods, but plays no significant role in the present work.

Two samples, hereafter named A and C, were prepared. Their surfaces are cut like faces A and C of Fig. 1, respectively. Note that the horizontal side of face C (tape-casting direction) is *roughly* the direction of the *c*-axis of the rods, while the vertical side of face C ('third' direction, i.e. normal to both the casting and the stacking directions) is *roughly* a 'thermal *a*-axis' direction. In a similar way, all directions in the plane of face A are *roughly* 'thermal *a*-axes'. The surface of both samples is coated with a 70 nm thick gold film to provide sufficient thermoreflectance signals.

Mirage measurements were performed on both samples A and C, for each one along the directions of the two sides. In other terms (Fig. 1), rectilinear sweeps were performed on sample C along the casting direction and along the 'third' direction. On sample A, sweeps were performed along the stacking direction and along the 'third' direction (orthogonal to both the casting and stacking directions). *Thermoreflectance microscopy* measurements were performed only in rods at the surface of sample C. A first series of data were taken in the *widest* rod present at the surface of sample C. The size of this rod (Fig. 2) is about 100 μm in length (*c*-axis direction) and 16·5 μm in width ('thermal *a*-axis' direction). Its depth is strictly speaking unknown. Yet the likeliest value is half

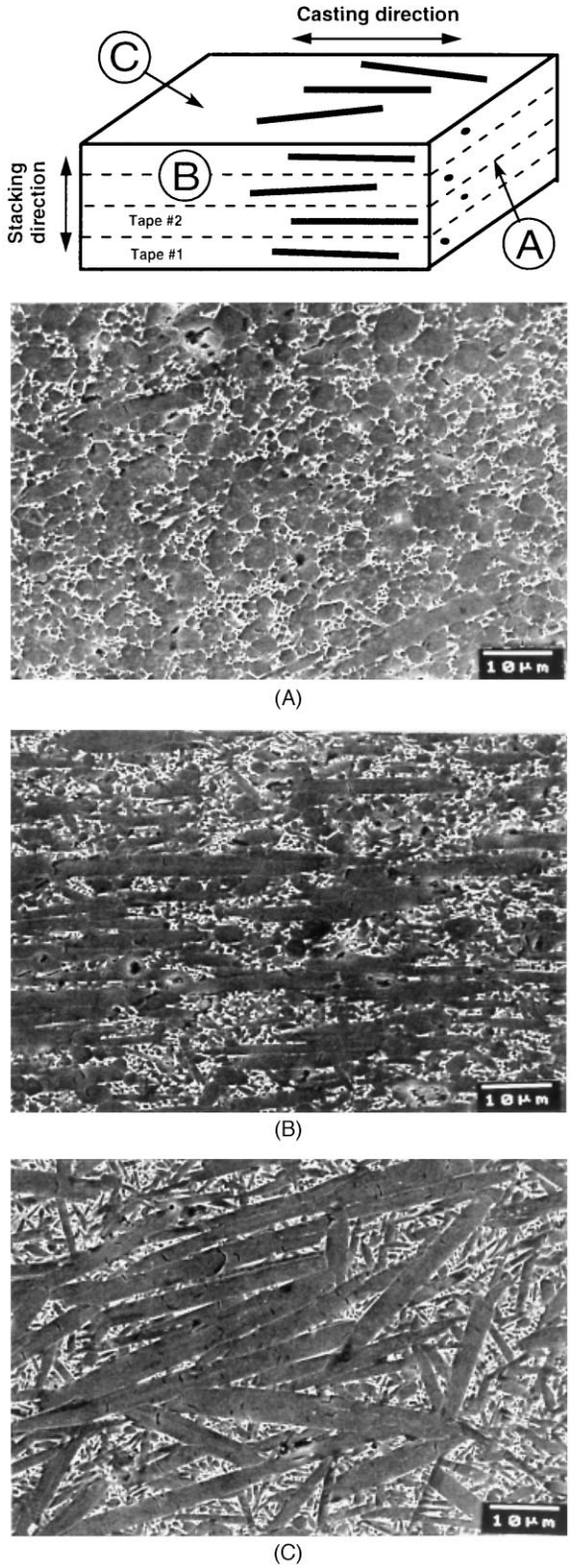

Fig. 1. The Si_3N_4 ceramic's microscopic structure. On the three scanning electron micrographs, the darker regions are the Si_3N_4 grains, the lighter regions are a second phase. Although the long β-Si_3N_4 rods are not perfect single crystals, their long axis is known[16] to coincide with the *c*-axis of the uniaxial (hexagonal) structure of β-Si_3N_4. The *c*-axes are thus oriented *approximately* along the casting direction—yet with a non-negligible dispersion.

the width (i.e. one radius) of the rod. Two principal thermal axes (*a*- and *c*-axis) lie in the surface plane. The measurements performed in this 'giant' rod were used to fit the principal diffusivities. A

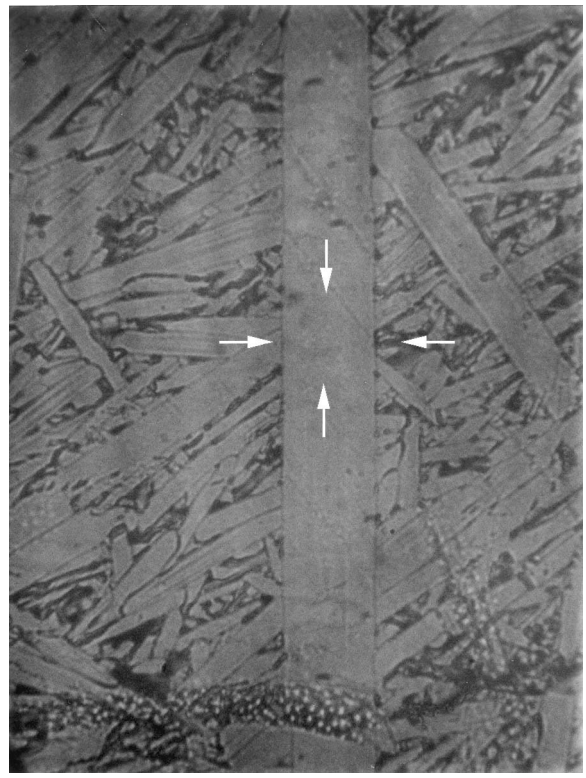

Fig. 2. Partial view of the widest Si_3N_4 rod on sample C's surface (optical microscope picture, retouched for better legibility). The *c*-axis is parallel to the edges of this very long rod. The four white arrows, point to the centre of the region of the measurements.

second series of measurements were then performed in rods of diameters ranging from 8 to 12 μm, as well as in regions where several parallel rods (of diameters from 3 to 6 μm) seem to be in tight contact. These measurements were used to cross-check the results obtained from the widest rod.

In the case of the rods on sample C, the *c*-axis and one *a*-axis of the diffusivity tensor are located in the surface plane. A *1D* scan of the heating focal spot is performed on the sample's surface, along a straight line that passes through the centre of the (fixed) focal probe spot. The direction of this straight line is chosen parallel to one, then to the other principal diffusivity direction of the rod in the surface plane. During each scan the amplitude and the phase of the thermoreflectance modulation are recorded versus the separation of the two laser spots.

In measurements of the widest rod, data were taken at five different modulation frequencies. To 'keep the thermal wave inside the rod', the frequency was always $\geq$100 kHz, so that the 'thermal *a*-axis' diffusion length (defined as $\mu = [D_a/\pi f]^{1/2}$, where D_a is the principal diffusivity along the *a*-axis and f is the modulation frequency of the heating beam) remained smaller than, or close to, the half width of the rod. The measurements at the five frequencies were used all at the same time in the fit to determine the principal diffusivities.

3 Theoretical Background for Thermoreflectance Measurements

Even though several theoretical treatments on thermal conduction in anisotropic materials are already available,[9,11,24] none of them is applicable to our system of isotropic film and anisotropic substrate, so we developed our own model. We consider a semi-infinite anisotropic substrate covered with an isotropic thin film of thickness l. Two principal axes of the anisotropic substrate are assumed to be located in the surface plane of the sample (x and y axes), while the third one is normal to the surface (z axis). The principal thermal conductivities and diffusivities of the substrate are K_{2x}, K_{2y}, K_{2z}, and D_{2x}, D_{2y}, D_{2z}, respectively. The sample is surrounded by air. The thermal conductivities and diffusivities of air and of the film are noted K_0, K_1, D_0 and D_1. We assume there is a thermal boundary resistance R_{th} at the film/substrate interface. We assume also that only the film absorbs energy from the heating beam and converts it into heat. The absorption coefficient of the film is called α_1. For a heating beam at normal incidence, the surface temperature rise can be written in $\{x, y\}$ Fourier transform representation as[9]

$$T(x, z, y=0, t) = \frac{1}{2}\int_{-\infty}^{\infty}\int_{-\infty}^{\infty} \mathrm{d}\delta\mathrm{d}\eta\big[A(\delta,\eta) + B(\delta,\eta) + E(\delta,\eta)\big]\exp\big[j(\delta x+\eta y)\big]\exp(j\omega t) + c.c. \tag{1}$$

Here $\omega = 2\pi f$ is the angular frequency of the heating beam, δ and η are the Fourier conjugates of x and y. For a heating beam of Gaussian profile,

$$E(\delta,\eta) = \frac{\alpha_1(1-R_1)P}{2\pi K_1}\exp\big(-(\delta^2+\eta^2)a^2/4\big)/\big(\beta_1^2-\alpha_1^2\big) \tag{2}$$

where R_1 is the surface reflectivity of the thin film, P is the power of the heating beam, and a is its ($1/e$)-radius. Quantities A, B and E are defined as

$$A(\delta,\eta) = \big\{(1-g_1)\big[s-g_2(1-bs)\big]\exp(-\alpha_1 l) - (g_1+s)\big[1+g_2(1+b)\big]\exp(\beta_1 l)\big\}\frac{E(\delta,\eta)}{H(\delta,\eta)} \tag{3a}$$

$$B(\delta,\eta) = \big\{(1+g_1)\big[s-g_2(1-bs)\big]\exp(-\alpha_1 l) - (g_1+s)\big[1-g_2(1-b)\big]\exp(-\beta_1 l)\big\}\frac{E(\delta,\eta)}{H(\delta,\eta)} \tag{3b}$$

with

$$H(\delta,\eta) = (1+g_1)[1+g_2(1+b)]\exp(\beta_1 l) - (1-g_1)[1-g_2(1-b)]\exp(-\beta_1 l) \tag{4}$$

$$\beta_i^2 = \delta^2+\eta^2+j\omega/D_i,\ (i=0,1) \tag{5a}$$

$$\beta_2^2 = \frac{1}{D_{2z}}\big[D_{2x}\delta^2 + D_{2y}\eta^2 + j\omega\big] \tag{5b}$$

and

$$g_1 = \frac{K_0\beta_0}{K_1\beta_1};\ g_2 = \frac{K_{2z}\beta_2}{K_1\beta_1};\ s = \frac{\alpha_1}{\beta_1};\ b = R_{th}K_1\beta_1 \tag{6}$$

Equations (1)–(6) express the temperature modulation at the surface of the film. In modulated thermoreflectance experiments, the measured signal is proportional to the temperature modulation. Therefore, eqn (1) is used directly to fit the measured signal.

4 Results and Discussion

First, the macroscopic thermal diffusivities of the Si_3N_4 ceramic samples were measured in mirage experiments. The thermal diffusivity was extracted from the slope $\mathrm{d}\phi/\mathrm{d}x$ of the phase ϕ of the transverse deflection of the probe beam as a function of the probe beam offset x using the 'phase method'.[11,18] The reported values are the averages of measurements at several modulation frequencies from 20 Hz to 2 kHz. Figure 3 shows an example of mirage results and the corresponding best fits[23] for both samples A and C. For sample A, we obtained a diffusivity of $0{\cdot}26\,\mathrm{cm^2\,s^{-1}}$ along the stacking direction, and of $0{\cdot}36\,\mathrm{cm^2\,s^{-1}}$ along the normal direction. For sample C the diffusivities measured in the casting direction and in the normal direction are $0{\cdot}54\,\mathrm{cm^2\,s^{-1}}$ and $0{\cdot}35\,\mathrm{cm^2\,s^{-1}}$, respectively.

To understand the thermal anisotropy revealed by the mirage experiments (as well as by laser flash measurements[16]), we measured heat diffusion inside individual Si_3N_4 grains by modulated thermoreflectance microscopy. First, we recorded the 2-dimensional phase maps of the thermoreflectance signals obtained on the widest rod (Fig. 2) at 1·0 MHz and 300 kHz, in a raster scan of the heating spot, with the probe spot fixed on the axis of the rod. At both frequencies the range of the thermal wave is short enough for the wave to remain inside the rod. The recorded phase maps are shown in Fig. 4. The horizontal direction in Fig. 4 corresponds to the axis of the rod (vertical direction of Fig. 2). The anisotropy is obvious. At the higher frequency, the penetration depth of the thermal wave is shorter. The contributions of the (isotropic) gold film and of the (also isotropic) thermal

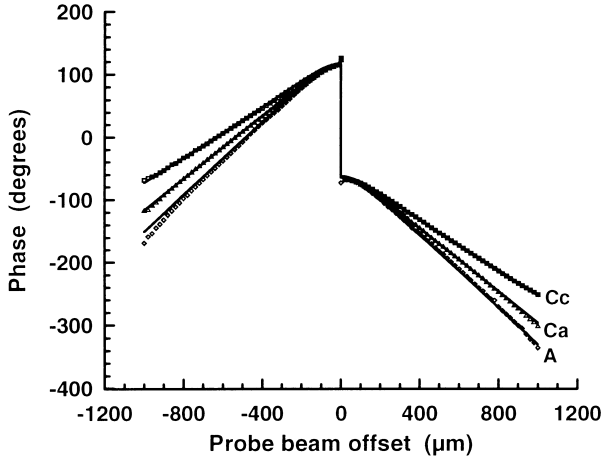

Fig. 3. Example mirage effect results: dependence of the transverse deflection's phase on the probe beam offset for sample A (curve A), for sample C along the casting direction (approximate *c*-axis direction; curve Cc), and for sample C along the direction normal to both the casting and the stacking directions (approximate 'thermal *a*-axis' direction; curve Ca). Experimental points (diamonds, triangles and squares), and theoretical predictions (solid lines) computed from the diffusivity values $D(A) = 0{\cdot}26\ \mathrm{cm^2\ s^{-1}}$, $D(Ca) = 0{\cdot}35\ \mathrm{cm^2\ s^{-1}}$ and $D(Cc) = 0{\cdot}54\ \mathrm{cm^2\ s^{-1}}$. The modulation frequency is here 213 Hz.

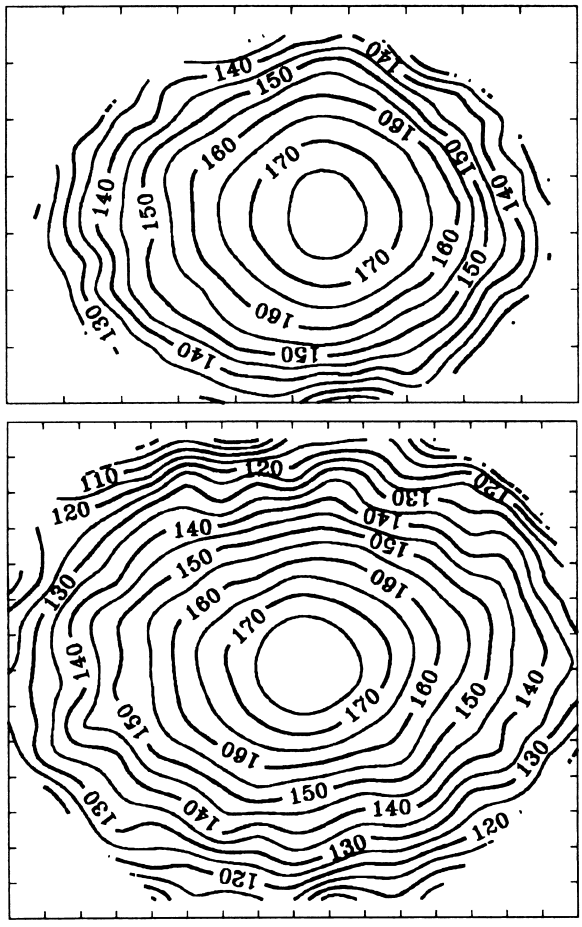

Fig. 4. Contour lines of the phase (in degrees) of the thermoreflectance signal. Heating beam's modulation frequency: 1·0 MHz (top) or 300 kHz (bottom). XY tick spacing: 1 μm. The centre of the pattern is the location of the centre of the (fixed) probe spot. For a given position $[X, Y]$ (in μm) of the centre of the heating spot, the map gives the corresponding phase $\Phi(X, Y)$. The space scale difference between the two maps originates in the longer thermal diffusion length at the lower frequency.

resistance are larger, while the contribution of the (anisotropic) substrate is smaller. This is why the phase map is less anisotropic at the higher frequency. The nearly circular shape of the phase contour line closest to either map's centre, is an effect of the (isotropic) thermal resistance and of the (circular) shape of the laser spots.

To determine the thermal diffusivities of the widest Si_3N_4 rod, the amplitude and the phase of the thermoreflectance signal were recorded as functions of the separation of the two spots along either of the two principal axes in the surface plane (i.e. *c*-axis and 'thermal *a*-axis'), at modulation frequencies of 0·1, 0·25, 0·5, 0·8, and 1·0 MHz. Figures 5 and 6 show the results measured at 0·80 and 0·25 MHz, together with the theoretical best fits. (Since the absolute calibration of the measured thermoreflectance modulation is not known, the amplitudes at each frequency were slightly rescaled—by factors of 0·8–1·0—to match the theoretical calculations.) Even at the lowest frequency (0·1 MHz) the measurements take place approximately 'inside the rod', so that the effect of the rod's walls on the measurements at all five frequencies is negligible. The principal thermal

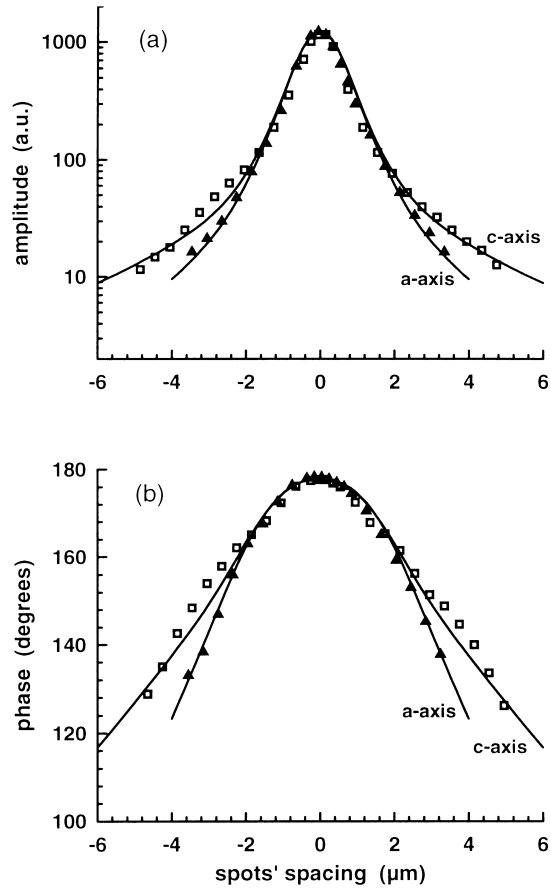

Fig. 5. Dependence of the amplitude (a) and of the phase (b) on the spacing between the heating and probe spots, along a 'thermal *a*-axis' or along the *c*-axis, for the widest Si_3N_4 rod. Modulation frequency: 800 kHz. Experimental points (triangles and squares) and theoretical best fit (solid lines).

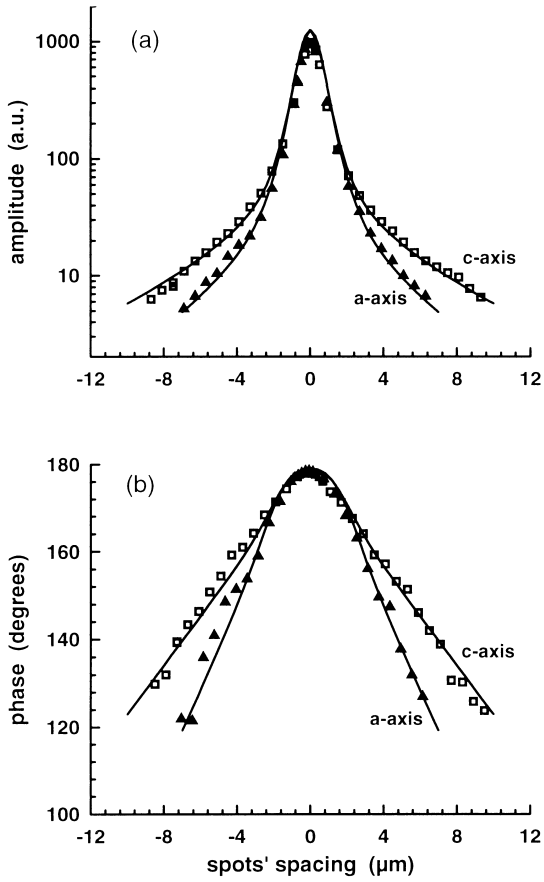

Fig. 6. Same as Fig. 5, except the modulation frequency is here 250 kHz.

diffusivities extracted from the best fits are $0{\cdot}32\,cm^2\,s^{-1}$ along the *a*-axis and $0{\cdot}84\,cm^2\,s^{-1}$ along the *c*-axis. The corresponding principal thermal conductivities $K = \rho CD$ are $69\,W\,m^{-1}\,K^{-1}$ and $180\,W\,m^{-1}\,K^{-1}$. (The bulk density ρ, measured by Archimedes' method in water, is $3205\,kg\,m^{-3}$. For the specific heat C we adopted a value of $670\,J\,K^{-1}\,kg^{-1}$, measured for sintered Si_3N_4 in a previous work[25] using the laser flash technique.) In the same fit, the thermal conductivity of the gold film is found to be $81\,W\,m^{-1}\,K^{-1}$ (i.e. only 0·26 time that of bulk gold), and the thermal boundary resistance turns out to be $4{\cdot}0\times10^{-8}\,m^2\,K\,W^{-1}$. On the other hand, because of the gold film and of the thermal resistance, the 'apparent thermal diffusivities' (i.e. the diffusivities extracted from the phase/separation slope using the simple formula $d\varphi/dr = -[\omega/2D]^{1/2}$) depend on the modulation frequency. In the low frequency region, for both principal axes the apparent value (deduced from the slope) is more than 20% lower than the best-fit result. This evidences, for the present case, the inadequacy of the simple 'slope method' and the need of fitting the theoretical model to all data simultaneously.

Measurements were also performed in other Si_3N_4 rods with 'thermal *a*-axis' lengths (i.e., radii) in the 8–12 μm range. For each rod, the minimum modulation frequency was kept high enough for the thermal wave to remain approximately inside the rod. That is, measurements were performed at 0·25, 0·5, and 1·0 MHz for rods of $\approx 12\,\mu$m, at 0·5 and 1·0 MHz for rods of $\approx 10\,\mu$m width. For rods of only $\approx 8\,\mu$m, measurements were performed only along the *c*-axis, at 0·1, 0·25, 0·5 and 1·0 MHz. All these measurements were compared to the theoretical calculations *using the same set of numerical values as obtained from the measurements in the widest Si_3N_4 rod*. But for a few discrepancies at 1·0 MHz, calculations and measurements are in good agreement.

The few discrepancies may originate in possible differences of the thermal properties of the gold coating and/or of the thermal resistance on different rods. (The higher the frequency, the larger the sensitivity to such differences.)

For still narrower Si_3N_4 rods, measurements were performed at 50, 100, 250 and 500 kHz, in 'bunches' consisting of several parallel rods ('thermal *a*-axis' size: 3–6 μm; bunch width: $\approx 20\,\mu$m) that seemed to be in tight contact. Again, the measurements were compared to the theoretical predictions using the *same set of numerical values* as previously. In the *c*-axis direction, good agreement was obtained at all frequencies. In the 'thermal *a*-axis' direction, on the other hand, the agreement depends noticeably on the thermal contact between the grains. For regions with negligible thermal barriers, good agreement is obtained in both amplitude and phase at all frequencies. Figure 7 shows the measured and theoretical results at 100 kHz for a bunch of four Si_3N_4 rods in tight, parallel arrangement. For regions of poor thermal contact between rods, some discrepancy appears between the measured results and the predictions calculated from the best-fit values. However, at all frequencies the overall slopes of the measured phase curves, which reflect the thermal quality of the material, remain very close to the slopes of the calculated phase curves. From all these measurements performed on Si_3N_4 rods of different diameters, we conclude that the Si_3N_4 rods possess an *intrinsic* thermal anisotropy, *independent of the rods' diameter*.

For a substrate coated with a thin film, at low modulation frequencies the amplitude and phase behaviour of the thermoreflectance signal is dominated by the thermal properties of the substrate. The effect of the film increases with the modulation frequency. Therefore, the results obtained at the *lowest* frequency (here, 100 kHz) are preferable when estimating the uncertainty of the measured *diffusivity of the Si_3N_4 rods*. On the other hand, the results at the *highest* frequency (here 1·0 MHz) are preferable when estimating the uncertainty of the

thermal boundary resistance and of the *diffusivity of the gold film*. The dashed lines of Fig. 7 show how the quality of the fit (at a frequency of 100 kHz) is affected by a ±10% change in the assumed values of the principal diffusivities of the rods. From Fig. 7 we conclude that the uncertainty of both estimated diffusivities of the Si_3N_4 grains is about ±10%. This is a reasonable uncertainty for a thermal diffusivity determination using photothermal methods. (The uncertainties were estimated in a similar way for the film's diffusivity and for the boundary resistance. Both amount to about ±25%.)

In contrast to a previously published opinion,[16] our measurements inside individual Si_3N_4 grains show that the Si_3N_4 grains are *intrinsically thermally anisotropic*. Our measured value of the *c*-axis conductivity ($180\,W\,m^{-1}\,K^{-1}$) turns out to be in excellent agreement with the value ($177\,W\,m^{-1}\,K^{-1}$) extrapolated, using the two-phase composite model, from laser flash measurements of the same tape-cast Si_3N_4 ceramic.[16]

We now turn our attention to the macroscopic diffusivities extracted from the mirage measurements. Figure 8 summarises the values D_{CC}, D_{NC}, D_{NA} and D_{SA} measured along the three directions (1st index: Casting, Stacking, or Normal to both), on either sample (2nd index: sample A or sample C). The values expected in the same three directions inside a single rod perfectly oriented along the casting direction (respectively: D_c, D_a and D_a again), are also recalled in Fig. 8, and we now give a qualitative interpretation of the differences between the macroscopic diffusivities and the single-rod ones.

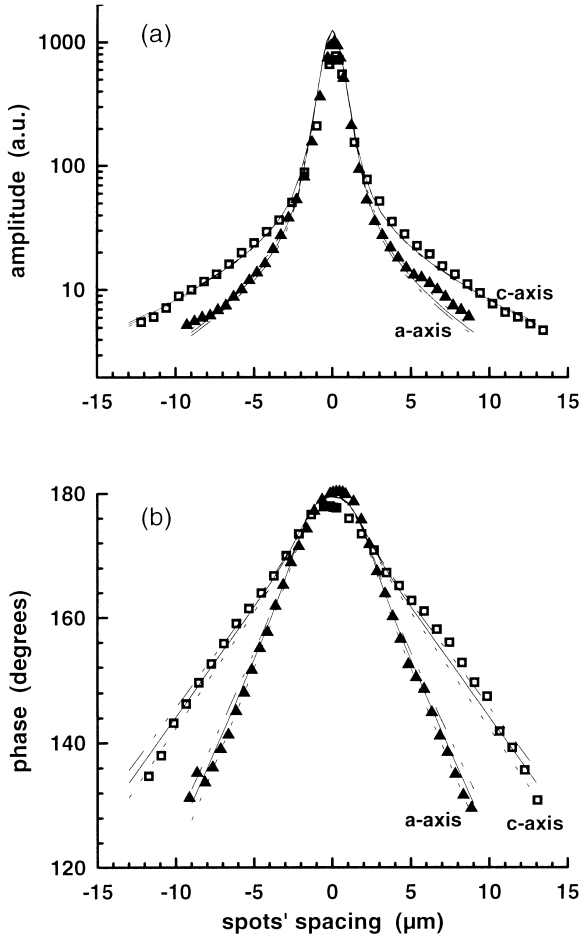

Fig. 7. Dependence of the amplitude (a) and of the phase (b) on the spacing between the heating and probe spots, along a 'thermal *a*-axis' or along the *c*-axis, in a bunch of four rods in tight, parallel arrangement. Modulation frequency: 100 kHz. Experimental points (triangles and squares), theoretical best fit (solid lines), and fits with modified conductivities (dashed lines) showing the sensitivity to the conductivities of the Si_3N_4 rods. The dashed lines labelled '*a*-axis' are the theoretical curves for a change of ±10% of the *a*-axis conductivity around the best-fit value ($69\,W\,m^{-1}\,K^{-1}$), with the *c*-axis/*a*-axis conductivity ratio kept constant. The dashed lines labelled '*c*-axis' are the theoretical curves for a change of ±10% of the *c*-axis conductivity around the best-fit value ($180\,W\,m^{-1}\,K^{-1}$), with the *a*-axis conductivity kept constant.

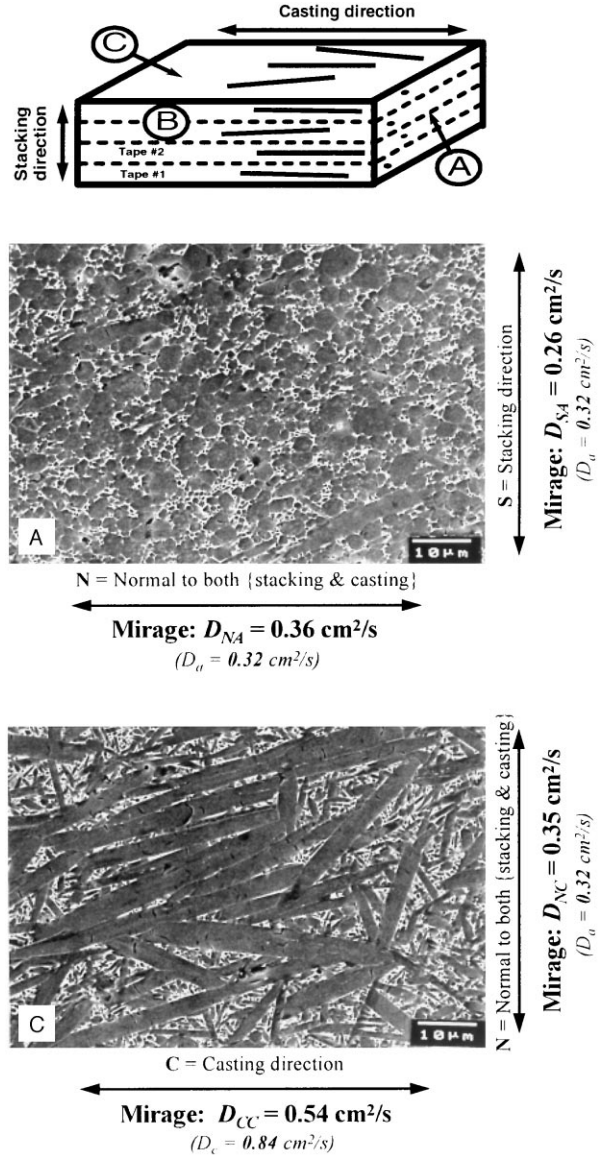

Fig. 8. Macroscopic diffusivity values measured by mirage effect, and comparison with the (parenthesised) corresponding values inside a single rod (assumed to be perfectly oriented along the casting direction).

The most salient difference is that the macroscopic diffusivity D_{CC} ($0{\cdot}54\,cm^2\,s^{-1}$) is much lower than the longitudinal diffusivity D_c ($0{\cdot}84\,cm^2\,s^{-1}$) inside a single rod. To explain this we see two causes:

1. The large dispersion of the rods' orientations around the casting direction in the plane of face C causes the macroscopic diffusivity D_{CC} along the casting direction to be lower than the diffusivity D_c along the *c*-axis inside a single rod, due to contamination by the much lower *a*-axis value D_a.
2. All macroscopic diffusivities contain a contribution from the second phase (mainly Y_2O_3 with small Si_3N_4 inclusions), whose diffusivity is lower than both D_c and D_a, as observed experimentally in a very similar material[16] (actually the 'latest previous generation' of the material studied here).

   The dispersion of the rods' orientations similarly explains why the macroscopic values D_{NA} ($0{\cdot}36\,cm^2\,s^{-1}$) and D_{NC} ($0{\cdot}35\,cm^2\,s^{-1}$) are larger than the transverse single-rod diffusivity D_a ($0{\cdot}32\,cm^2\,s^{-1}$): First, within the measurements uncertainties, the values of D_{NA} and D_{NC} are equal, as expected since either represents the macroscopic thermal diffusivity along direction *N*. Then, again because of the rods' orientation dispersion, diffusivity $\{D_{NA} = D_{NC}\}$ is larger than the transverse diffusivity D_a inside a single rod, due to contamination by the larger *c*-axis value D_c.

   At last, the contribution from the low diffusivity of the second phase also explains why the macroscopic diffusivity D_{SA} along the stacking direction ($0{\cdot}26\,cm^2\,s^{-1}$) is *smaller* than the transverse diffusivity D_a inside a single rod ($0{\cdot}32\,cm^2\,s^{-1}$) *despite the rods' orientation dispersion* in the plane of face B: since this dispersion is small (Fig. 1, micrograph B), its increase effect is dominated by the decrease effect of the second phase.

   As a conclusion of the above comparison, the differences between the macroscopic diffusivities and the single-rod ones turn out to be quite understandable.

5 Conclusion

Using high-resolution thermoreflectance microscopy, thermal anisotropy inside individual, rod-shaped Si_3N_4 grains in a ceramic has been evidenced, and the principal diffusivities have been determined. The spurious effects of the necessary gold film and of the thermal resistance at the film/substrate interface, were minimised by fitting the theoretical model's parameters at several frequencies simultaneously. Measurements in rods of different diameters have shown the thermal diffusivities of the Si_3N_4 rods to be independent of the diameters of the rods. Experimental evidence has been obtained that the Si_3N_4 rods of different diameters exhibit intrinsic thermal anisotropy. The three macroscopic principal diffusivities of this Si_3N_4-based ceramic have been measured by the mirage technique.

Acknowledgements

One of us (B.L.) gratefully acknowledges financial support from the CNRS-K.C. Wong foundation.

References

1. Anthony, T. R., Banholzer, W. F., Fleischer, J. F., Wei, L., Kuo, P. K., Thomas, R. L. and Pryor, R. W., Thermal diffusivity of isotopically enriched ^{12}C diamond. *Phys. Rev. B*, 1990, **42**, 1104–1111.
2. Salazar, A. and Sánchez-Lavega, A., Thermal diffusivity measurements using linear relations from photothermal wave experiments. *Rev. Sci. Instrum.*, 1994, **65**, 2896–2900.
3. Fabbri, L. and Fenici, P., Three-dimensional photothermal radiometry for the determination of the thermal diffusivity of solids. *Rev. Sci. Instrum.*, 1995, **66**, 3593–3600.
4. Roger, J. P., Lepoutre, F., Fournier, D. and Boccara, A. C., Thermal diffusivity measurement of micron-thick semiconductor films by mirage detection. *Thin Solid Films*, 1987, **155**, 165–174.
5. Wong, P. K., Fung, P. C. W., Tam, H. L. and Gao, J., Thermal-diffusivity measurements of an oriented superconducting-film–substrate composite using the mirage technique. *Phys. Rev. B*, 1995, **51**, 523–533.
6. Langer, G., Hartmann, J. and Reichling, M., Thermal conductivity of thin metallic films measured by photothermal profile analysis. *Rev. Sci. Instrum.*, 1997, **68**, 1510–1513.
7. Gan, Changming and Zhang, Xiaorong, Investigation of anisotropic thermal diffusivity using the 'mirage effect'. In *Photoacoustic and Photothermal Phenomena*, Vol. 58, Springer Series in Optical Sciences, ed. P. Hess. Springer Verlag, Berlin, 1988, pp. 335–338.
8. Rantala, J., Jaarinen, J. and Kuo, P. K., The effects of experimental parameters in the thermal diffusivity measurements of oriented polymer films using mirage effect: computer simulation. *Appl. Phys. A*, 1992, **55**, 586–595.
9. Quelin, X., Perrin, B., Louis, G. and Peretti, P., Three-dimensional thermal-conductivity-tensor measurement of a polymer crystal by photothermal probe-beam deflection. *Phys. Rev. B*, 1993, **48**, 3677–3682.
10. Bertolotti, M., Ferrari, A., Liakhou, G. L., Li Voti, R., Marras, A., Ezquerra, T. A. and Balta-Calleja, F. J., Thermal anisotropy of polymer carbon fibre composites as revealed by photodeflection methods. *J. Appl. Phys.*, 1995, **78**, 5706–5712.
11. Salazar, A., Sánchez-Lavega, A., Ocáriz, A., Guitonny, J., Pandey, G. C., Fournier, D. and Boccara, A. C., Thermal diffusivity of anisotropic materials by photothermal methods. *J. Appl. Phys.*, 1996, **79**, 3984–3993.
12. Hartmann, J., Voigt, P., Reichling, M. and Matthias, E., Photothermal measurement of thermal anisotropy in pyrolytic graphite. *Appl. Phys. B*, 1996, **62**, 493–497.

13. Salazar, A., Sánchez-Lavega, A. and Ocáriz, A., Photothermal characterisation of anisotropic materials with buried principal axes. *Opt. Eng. Bellingham (USA)*, 1997, **36**, 391–399.
14. Haggerty, J. S. and Lightfoot, A., Opportunities for enhancing the thermal conductivities of SiC and Si_3N_4 ceramics through improved processing. *Ceram. Eng. Sci. Proc.*, 1995, **16**, 475–487.
15. Hirosaki, N., Okamoto, Y., Ando, M., Munakata, F. and Akimune, Y., Thermal conductivity of gas-pressure-sintered silicon nitride. *J. Am. Ceram. Soc.*, 1996, **79**, 2878–2882.
16. Hirao, K., Watari, K., Brito, M. E., Toriyama, M. and Kanzaki, S., High thermal conductivity in silicon nitride with anisotropic microstructure. *J. Am. Ceram. Soc.*, 1996, **79**, 2485–2488.
17. Watari, K., Hirao, K., Brito, M. E., Toriyama, M. and Kanzaki, S., Hot-isostatic-pressing to increase thermal conductivity of Si_3N_4 ceramics. *J. Mater. Res.*, in press.
18. Bertolotti, M., Li Voti, R., Liakhou, G. and Sibilia, C., On the photodeflection method applied to low thermal diffusivity measurements. *Rev. Sci. Instrum.*, 1993, **64**, 1576–1583.
19. Pottier, L., Micrometer scale visualisation of thermal waves by photoreflectance microscopy. *Appl. Phys. Lett.*, 1994, **64**, 1618–1619.
20. Plamann, K., Fournier, D., Forget, B. C. and Boccara, A. C., Microscopic measurements of the local heat conduction in polycrystalline diamond films. *Diamond and Related Materials*, 1996, **5**, 699–705.
21. Fabbri, L., Fournier, D., Pottier, L. and Esposito, L., Analysis of local heat transfer properties of tape-cast AlN ceramics using photothermal reflectance microscopy. *J. Mater. Sci.*, 1996, **31**, 5429–5436.
22. Boccara, A. C., Fournier, D. and Badoz, J., Thermo-optical spectroscopy: detection by the 'mirage effect'. *Appl. Phys. Lett.*, 1980, **36**, 130–132.
23. Fournier, D. and Plamann, K., Thermal measurements on diamond and related materials. *Diamond and Related Materials*, 1995, **4**, 809–819.
24. Grönbeck, H. and Reichling, M., Harmonic heat flow in anisotropic thin films. *J. Appl. Phys.*, 1995, **78**, 6408–6413.
25. Watari, K., Seki, Y. and Ishizaki, K., Temperature dependence of thermal coefficients for HIPed silicon nitride. *J. Ceram. Soc. Japan*, 1989, **97**, 174–181.